Crystal structure, magnetic ordering, and magnetic excitation in the 4*f*-localized ferromagnet $CeAgSb_2$

Shingo Araki,[1,*] Naoto Metoki,[1,2] Andrei Galatanu,[1] Etsuji Yamamoto,[1] Arumugam Thamizhavel,[3] and Yoshichika Ōnuki[1,3]
[1]*Advanced Science Research Center, Japan Atomic Energy Research Institute, Tokai, Ibaraki 319-1195, Japan*
[2]*Department of Physics, Tohoku University, Aoba, Sendai 980-8578, Japan*
[3]*Graduate School of Science, Osaka University, Toyonaka, Osaka 560-0043, Japan*
(Received 30 October 2002; revised manuscript received 10 February 2003; published 10 July 2003)

Systematic neutron-scattering experiments have been carried out in order to reveal the crystal and magnetic structures as well as the magnetic excitation in the Ce-based intermetallic compound $CeAgSb_2$. It was clarified that the Ag atoms in $CeAgSb_2$ (space group: P4/*nmm*) occupy the 2*b* site, while Sb atoms occupy 2*a* and 2*c* sites, which have, to date, been controversial in literature. From the analysis of neutron powder-diffraction profile, we found the existence of the ferromagnetic component of about $0.41\mu_B$/Ce oriented along the *c* axis, consistent with the result of previous studies. On the other hand, however, no trace of the antiferromagnetic or spin-density wave peak was detected within our range of experimental accuracy. We observed a considerable spin-wave excitation below 3 meV. The dispersion relation was explained by the anisotropic Heisenberg model. This means that $CeAgSb_2$ has a simple ferromagnetic structure. Furthermore, crystalline electric-field (CEF) excitations were observed at 5.2 and 12.5 meV in the paramagnetic state, which is indicative of the localized nature of the Ce-4*f* electron. Our analysis revealed that $|J_z=\pm\frac{1}{2}\rangle$ is the ground state, while the first and second excited levels are mainly due to $|\pm\frac{3}{2}\rangle$ and $|\pm\frac{5}{2}\rangle$, respectively. The observed ferromagnetic moment is in good agreement with the ground-state saturation moment, $g_J\mu_B J_z \sim 0.43\mu_B$. The susceptibility, magnetization curve, and magnetostriction can be explained in terms of the CEF level scheme with anisotropic exchange interaction.

DOI: 10.1103/PhysRevB.68.024408 PACS number(s): 75.20.Hr, 71.27.+a, 61.12.Ld, 78.70.Nx

I. INTRODUCTION

Ferromagnetic materials based on *f* electrons are attracting renewed interest in the study of unconventional superconductivity coexisting with ferromagnetism. The study of ferromagnetic superconductivity has a long history, beginning with Ginzburg's study in 1957 (Ref. 1). Recently, ferromagnetic superconductivity was discovered in UGe_2 (Ref. 2) and URhGe (Ref. 3). After the significant discovery of ferromagnetic superconductivity in the case of UGe_2 and URhGe, a number of compounds have been investigated, but most of these efforts have been unsuccessful. The absence of ferromagnetic superconductivity is discussed, e.g., in terms of the lack of inversion symmetry as well as an insufficient sample quality. However, at the same time, these efforts shed light on unusual and interesting magnetic properties of ferromagnets based on *f* electrons.

$CeAgSb_2$ is one of the materials that order at $T_c \simeq 9$ K, with a small net ferromagnetic component of $0.33\mu_B$/Ce (Ref. 4). The γ coefficient of specific heat, 75 mJ/K^2 mol, is enhanced compared to that of $LaAbSb_2$, 2.62 mJ/K^2 mol (Ref. 5). The magnetic ordering can be easily suppressed with the application of pressure of about 3.3 GPa. No superconductivity has been reported down to 90 mK, even in a high-quality single crystal with the residual resistivity ratio $\rho_{RT}/\rho_0 = 1700$ for $\boldsymbol{J}\|[001]$ (Ref. 6).

Other than the high-pressure response, the unusual magnetic properties in $CeAgSb_2$ have not yet been understood. First, the magnetic susceptibility perpendicular to [001] is larger than that parallel to [001]. However, the magnetic ordered moment below T_c is parallel to the *c* axis. Second, the hard-axis magnetization below T_c increases linearly with magnetic field and reaches about 1.2 μ_B at 3 T (Ref. 7). This induced moment is much larger than the spontaneous moment along the *c* axis, $0.4\mu_B$. The antiferromagnetic (AFM) and/or complex magnetic structure was believed to be the origin of the unusual magnetic properties. However, no AFM peak has been reported, to date, from neutron diffraction experiments.[4] Very recently, the study of thermal and magnetic properties revealed that the magnetic susceptibility could be explained by the crystalline electric-field (CEF) effect.[8,9] It was also revealed that the saturation moment can be understood in terms of the $|J_z=\pm\frac{1}{2}\rangle$ ground state, although the reason why the ferromagnetic component is parallel to the *c* axis remains an open question.

The purpose of this neutron-scattering study is to clarify the crystal and magnetic structure as well as magnetic excitations in $CeAgSb_2$ in order to understand the unusual magnetic properties of this compound. We conclude that $CeAgSb_2$ has a simple ferromagnetic ground state. We introduce an anisotropic ferromagnetic interaction which systematically explains the unusual magnetic properties in $CeAgSb_2$.

II. EXPERIMENTAL DETAILS

A polycrystalline sample was prepared by arc-melting of the constituent elements. The starting materials were 3N (99.9% pure) Ce, 4N Ag, and 5N Sb, at the ratio of 1:1:2.4 to compensate for the loss of antimony due to evaporation. The arc-melted sample was annealed in an evacuated quartz tube at 600 °C for one week. The quality of samples was

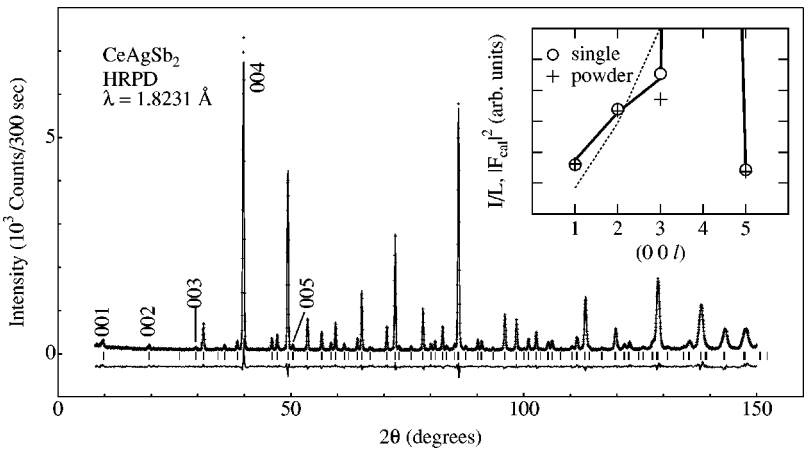

FIG. 1. Neutron powder-diffraction pattern at room temperature in $CeAgSb_2$. The inset shows the integrated intensities of the $(00l)$ ($l=1$, 2, 3, and 5) reflections on a single-crystal (open circles) and polycrystalline sample (crosses) measured at 12 K. The bold line and dashed line denote the square of the structure factor, calculated based on the Sologub-type structure and André-type structure, respectively.

examined by x-ray (Cu Kα) and neutron powder diffraction studies. No trace of impurity phases was detected. The diffraction profile was interpreted by that of stoichiometric $CeAgSb_2$. The deviations from the full occupancies of each atomic site was estimated to be less than 3%. The well-grained sample was encapsuled in a very thin vanadium tube, and sealed in an aluminum can with He gas. The total mass of the polycrystalline sample was about 30 g. On the other hand, single crystals were grown by the Sb-self-flux method. The starting materials were again 3N Ce, 4N Ag, and 5N Sb. Typical sample dimensions were $15\times7\times2.5$ mm^3 with a weight of 0.85 g. A sample was mounted on an aluminum sample holder and sealed in an aluminum can with He gas. The $(hk0)$, $(h0l)$, and (hhl) planes were scanned in order to observe magnetic reflections.

Neutron-scattering experiments were carried out at the research reactor JRR-3 at the Japan Atomic Energy Research Institute. High resolution neutron powder-diffraction data were measured on high resolution power diffractometer (HRPD) installed at the 1G port in the reactor hall. A thermal neutron beam with wavelength $\lambda=1.8231$ Å was monochromatized by a Ge(331) monochromator. A typical angle resolution was obtained by collimating the neutron beam with $6'$-$12'$-$6'$ collimators. Powder-diffraction experiments were also carried out on a thermal triple-axis spectrometer TAS-1 in order to obtain good statistics in the integrated intensity of the low-angle diffraction peaks. The neutron beam was monochromatized at 14.7 meV and analyzed using vertically bent pyrolytic graphite (PG) crystals. Higher-order contamination was removed by a PG filter with a thickness of 8 cm. The angle resolution of TAS-1 was about $\simeq0.5°$ with the collimation of $40'$-$80'$-$40'$-$80'$. Magnetic reflection was also searched for using a single-crystalline sample on thermal triple-axis spectrometers TAS-1 and TAS-2. TAS-2 is installed at the T2-4 beam port located at the end position of the 3q supermirror guide in the guide hall of JRR-3. A large neutron beam, 20 cm in height and 2 cm in width, was focused on the sample using a vertically bent monochromator at the energy of 14.7 meV, and analyzed using a PG analyzer. The collimation was $80'$-$40'$-$80'$. A PG filter was used to remove harmonic contaminations. Neutron inelastic scattering spectra were measured using TAS-1 at final energies $E_f=14.7$ and 30.5 meV, which provide the energy widths of vanadium incoherent scattering of about 1 meV and 3 meV, respectively. The low-energy excitations were also measured with low energy triple-axis spectrometer (LTAS) with a cold neutron beam at $E_f=4$ meV.

III. EXPERIMENTAL RESULTS

A. Crystal Structure

$CeAgSb_2$ crystallizes in the tetragonal structure with space group P4/nmm. Two controversial models have been proposed so far for the crystal structure of $CeAgSb_2$. Sologub *et al.*[10] and Brylak, Moller, and Jeitschko[11] reported that $CeAgSb_2$ has a $ZrCuSi_2$-type structure, where Ce, Ag, and Sb atoms occupy the crystallographical 2c (Ce), 2b (Ag), 2a (Sb1), and 2c (Sb2) sites. On the other hand, André *et al.*[4] attributed their neutron powder-diffraction data to the same type of structure, but assumed different site occupations, namely, 2a (Ag) and 2b (Sb1) sites. This controversy is due to the weak contrast between Ag and Sb atoms, both for x-rays and neutrons.

Figure 1 shows the high-resolution neutron powder-diffraction data of $CeAgSb_2$ measured at room temperature in the paramagnetic state. This powder-diffraction data can be explained by both Sologub- and André-type structures, although reliable parameters for Sologub's model are slightly better than the ones for André's model. In order to clarify the crystal structure of $CeAgSb_2$, the weak (001), (002), (003), and (005) reflections from a large polycrystalline sample (30 g) and a high-quality single-crystalline sample were mea-

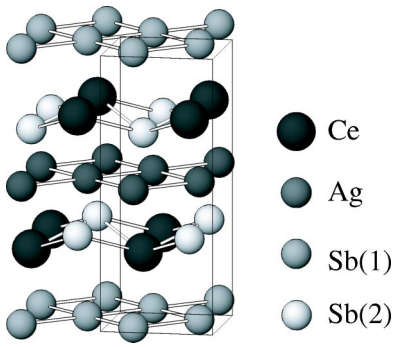

FIG. 2. Crystal structure of $CeAgSb_2$. The solid line indicates the tetragonal unit cell.

TABLE I. Crystallographic data in $CeAgSb_2$ obtained by Rietveld refinement of neutron powder-diffraction data in Fig. 1.

$a=4.3675(4)$ Å, $c=10.708(1)$ Å, $B=0.65(1)$ Å^2 $R_{wp}=7.25\%$ ($R_e=6.81\%$), $R_I=3.25\%$				
Atom	Site	x	y	z
Ce	2c	1/4	1/4	0.2388(2)
Ag	2b	3/4	1/4	1/2
Sb1	2a	3/4	1/4	0
Sb2	2c	1/4	1/4	0.6734(3)

sured with very good statistics on the TAS-1 spectrometer. The stacking sequence of the atomic layers along the c axis is Ce-Sb-Ag-Sb-Ce-Sb-Ce in Sologub's model, while it is different from that of André's model, Ce-Sb-Sb-Sb-Ce-Ag-Ce. Therefore, the envelope of the $(00l)$ peak intensity is effective for distinguishing these models. The observed integrated intensities of $(00l)$ reflections for $l=1$, 2, 3, and 5 are plotted in the inset of Fig. 1. The polycrystalline (crosses) and single-crystalline (open circles) data are consistent. The agreement of the experimental data with the calculated intensity for Sologub's model (solid line) is clearly better than that of André's model denoted by the dashed line, as shown in the inset of Fig. 1. Therefore, we conclude that Sologub's model describes the crystal structure of $CeAgSb_2$, which is schematically shown in Fig. 2. In this structure, Ce atoms show a quasi-body-centered tetragonal lattice. The local arrangements of Ce and Sb atoms are very similar to those of $CeSb_2$. In $CeAgSb_2$, the $CeSb_2$ layer is separated by an Ag layer.

Our conclusion for the crystal structure of $CeAgSb_2$ is acceptable because the series of $CeTSb_2$ (T: Ni, Pd, Cu, Au) compounds have the same crystal structure as described by Sologub's model.[10,12] This has been unambiguously confirmed by the diffraction experiments of $CeTSb_2$, in which strong contrast was observed between T and Sb atoms. The high-resolution neutron powder-diffraction pattern in Fig. 1 was analyzed by means of Rietveld refinement with RIETAN-2000,[13] assuming Sologub's model. The fit of the data is satisfactory. The obtained structural parameters are listed in Table I.

Recently, Fujimori *et al.*[14] reported that the *d*-electron density of states observed by photoemission spectroscopy is consistent with the band calculation based on the Sologub-type structure. Their conclusion is in good agreement with the result of the present neutron-scattering study.

B. Magnetic Structure

Figure 3 shows the neutron powder-diffraction pattern at $T=4$ K and 12 K, which are below and above the Curie temperature $T_c=9.6$ K, respectively. The low-temperature data, after subtracting the high-temperature data, are also plotted in Fig. 3. The clear ferromagnetic scattering from Ce moments were superposed on the (101) and (110) nuclear peaks. The ferromagnetic scattering on the (103) and (112) nuclear peaks may also be observed, which are, however, masked by the large nuclear scattering. Some small cusp-like structure, e.g., $2\theta=36°$, seen in Fig. 3, were investigated again with higher statics, however, these peak structures were not reproducible. Therefore, we conclude that no antiferromagnetic scattering was observed in our experiment. The magnetic scattering intensity can be described by

$$I \propto \mu^2 |f(\boldsymbol{q})|^2 |F_{\mathrm{Ce}}|^2 \sin^2\theta L(\theta), \tag{1}$$

where μ is the magnetic moment of Ce^{3+}, $f(\boldsymbol{q})$ is the magnetic form factor of Ce^{3+} ion, F_{Ce} is the structure factor of Ce atoms, θ describes the angle between the magnetic moment and scattering plane, and $L(\theta)$ is the Lorentz factor. The inset of Fig. 3 shows the integrated intensity divided by the Lorentz factor. The observed data can be explained by the ferromagnetic component of $0.41(3)\mu_B$ parallel to the c axis. This is consistent with previous neutron-scattering and magnetization studies.[4,7,15] Although the statistical error of our neutron powder-diffraction data is much smaller than that in the previous study,[4] we could observe no trace of antiferromagnetic or incommensurate magnetic satellite

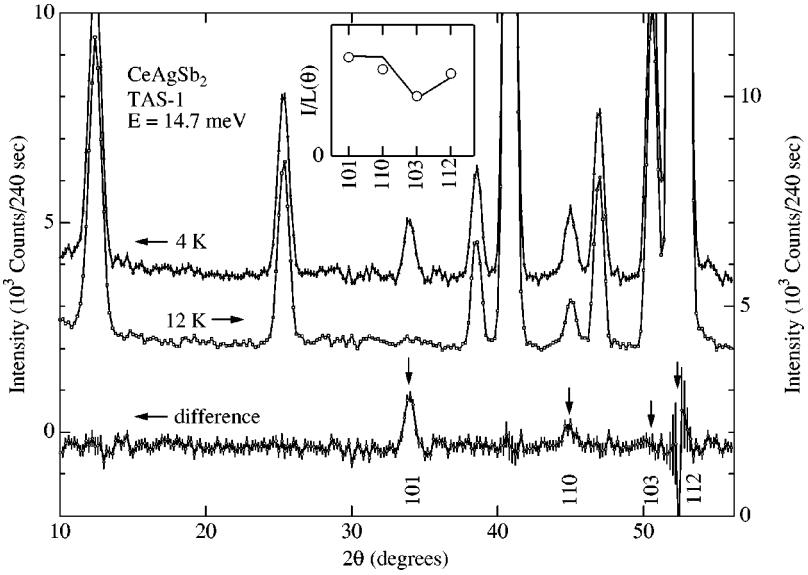

FIG. 3. Neutron powder-diffraction patterns below (4 K) and above (12 K) $T_c=9.6$ K in $CeAgSb_2$. The magnetic diffraction pattern which is obtained as the difference of patterns between 4 K and 12 K, is also plotted. The negative background for the subtracted data is due to the paramagnetic scattering at 12 K. The inset shows the integrated intensity of the magnetic scattering.

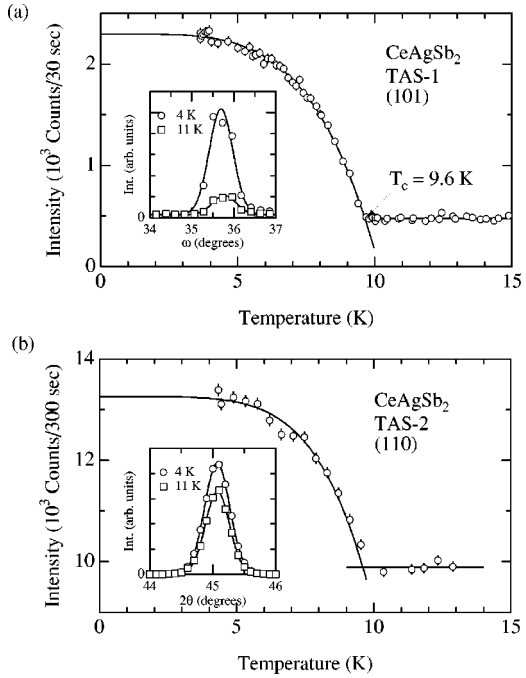

FIG. 4. Temperature dependence of (a) (101) and (b) (110) reflection intensity in $CeAgSb_2$. The insets show the scattering profiles below and above T_c.

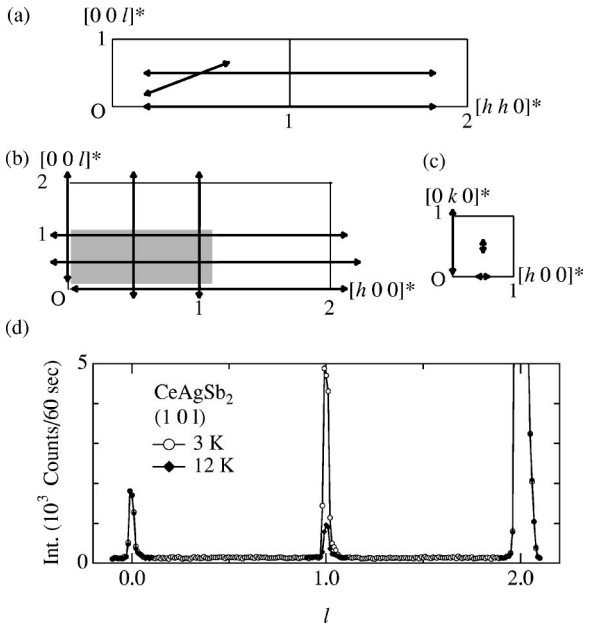

FIG. 5. Magnetic scattering from a single-crystalline sample of $CeAgSb_2$ is searched for, along some high-symmetry axes in the (a) (hhl), (b) $(h0l)$, and (c) $(hk0)$ planes denoted by the arrows and gray region. (d) Typical constant-energy scan along $[10l]$.

peaks within the accuracy range of the statistical error of the background $\sqrt{4000}=63$ counts, which roughly corresponds to 5×10^{-2} of the (101) ferromagnetic intensity. This result rules out the possibility of a primitive antiferromagnetic component in the order of $0.41\mu_B\times\sqrt{5\times10^{-2}}=0.09\mu_B$/Ce. If we assume a long-wavelength antiferromagnetic modulation M with N spins in a period, the intensity is proportional to $(M/N)^2$, hence the upper limit of the modulation is, roughly speaking, on the order of $0.09\times(N/M)\mu_B$/Ce. This value is also much smaller than the in-plane antiferromagnetic component on the order of $1\mu_B$ expected from the magnetization measurements.

The neutron elastic-scattering experiments have also been carried out using a single-crystal sample. We observed strong ferromagnetic scattering at the (101) and (110) nuclear peak positions. The temperature dependence plots of the (101) and (110) peak intensities are shown in Fig. 4. The peak intensity clearly exhibits a nature of the ferromagnetic order parameter with ordering temperature $T_c=9.6$ K. This is consistent with the previous results.[4,7] The (101) and (110) scattering profiles are also shown in the inset of Fig. 4. These results for a single-crystalline sample were consistent with the results for the polycrystalline sample.

An antiferromagnetic peak was searched for in the case of the single-crystalline sample. Although the diffraction experiments with a single crystal presents a much higher sensitivity with low background, no trace of the antiferromagnetic peak was observed in the accuracy range of 3×10^{-3} of the (101) ferromagnetic peak along some high-symmetry axes on the (hhl), $(h0l)$, and $(hk0)$ scattering planes, as shown in Figs. 5(a), 5(b), and 5(c), respectively. The sensitivity was $0.02\mu_B$/Ce. A typical example of our scattering profile along $(10l)$ is shown in Fig. 5(d). We also performed a mesh scan on the $(h0l)$ scattering plane, as shown in the hatched area in Fig. 5(b). However, no antiferromagnetic or spin-density wave (SDW) peak was detected.

C. Magnetic Excitation

Figure 6 shows the neutron inelastic-scattering spectra on the polycrystalline sample of $CeAgSb_2$. At $T=4$ K, we observed conspicuous excitation peaks at the neutron energy transfer $\Delta E=1.9$ and 5.9 meV, respectively. The $\boldsymbol{q}$ dependence of the intensity of these peaks is more or less consistent with the square of the $4f$ magnetic form factor in the Ce^{3+} ion. This means that these inelastic peaks are due to magnetic excitations. On elevating the sample temperature to $T=12$ K, just above $T_c=9.6$ K, the excitation peak at 1.9 meV disappeared. This means that this peak is due to the spin-wave excitation. The 5.2 meV peak, which corresponds to the 5.9 meV excitation at 4 K, survived in the paramagnetic state, although the peak became weak and broad. At a much higher temperature $T=60$ K, the excitation peak spreads out in a wide energy range. From $\boldsymbol{q}$ and temperature dependence, we concluded that the 5.2 meV peak is due to CEF excitation. In addition to these clear excitation peaks, a very weak excitation at $\Delta E=12.5$ meV was observed at 12 K, as shown in Fig. 7. Recently, these two CEF excitations were also observed by Adroja *et al.* on a HET spectrometer at ISIS, independent of our work.[16]

The CEF Hamiltonian for the tetragonal symmetry can be expressed as[17]

$$\mathcal{H}_{CEF}=B_2^0\boldsymbol{O}_2^0+B_4^0\boldsymbol{O}_4^0+B_4^4\boldsymbol{O}_4^4, \quad (2)$$

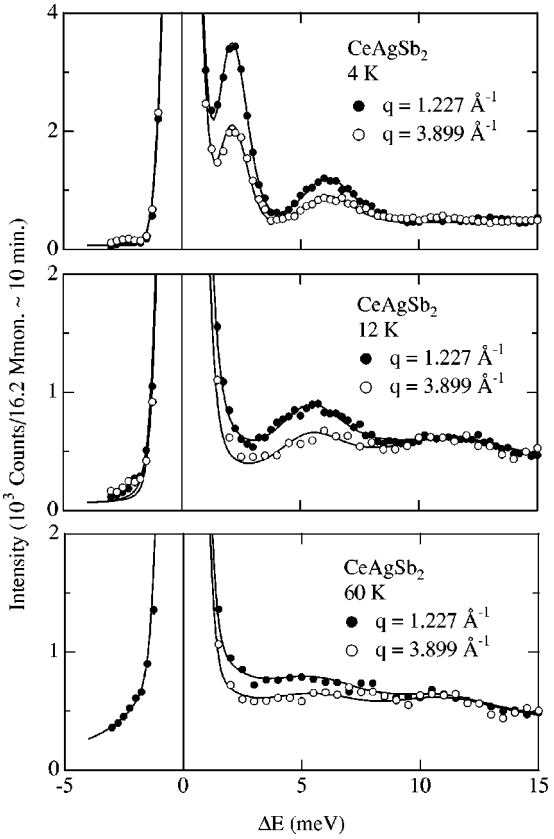

FIG. 6. Inelastic neutron-scattering spectra measured for a polycrystalline sample of $CeAgSb_2$.

where B_n^m and $\boldsymbol{O}_n^m$ are CEF parameters and Steven's operators,[18] respectively. In CEF with tetragonal symmetry, the J multiplet of the Ce^{3+} ion splits into three doublets,

$$|\Gamma_7^{(2)}\rangle = a\left|\pm\frac{5}{2}\right\rangle + b\left|\mp\frac{3}{2}\right\rangle, \tag{3}$$

$$|\Gamma_7^{(1)}\rangle = a\left|\pm\frac{3}{2}\right\rangle - b\left|\mp\frac{5}{2}\right\rangle, \tag{4}$$

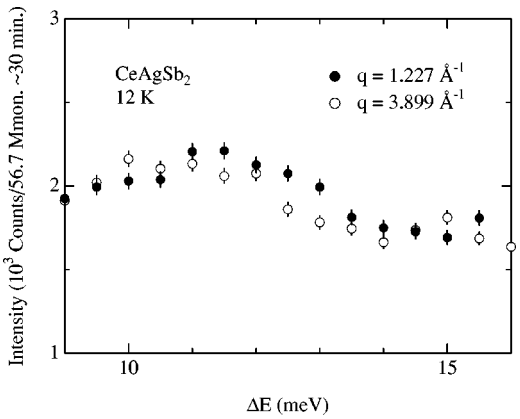

FIG. 7. Inelastic neutron-scattering spectra around 12 meV measured for a polycrystalline sample of $CeAgSb_2$.

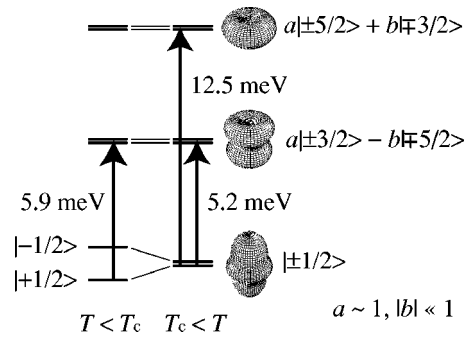

FIG. 8. CEF level scheme of $CeAgSb_2$ determined by the present neutron-scattering experiments. The charge distribution of each level is also shown at the right-hand side of the level scheme.

$$|\Gamma_6\rangle = \left|\pm\frac{1}{2}\right\rangle. \tag{5}$$

Therefore, the observation of two CEF excitation peaks is reasonably understood in terms of the excitation between the ground state and the two excited levels.

The neutron-scattering cross section for CEF level splitting can be described as

$$S(\boldsymbol{q},\omega) \propto |f(\boldsymbol{q})|^2 \sum_{nm} \rho_m |\langle n|J_\perp|m\rangle|^2 \delta(\omega - \Delta_{nm}), \tag{6}$$

where $f(\boldsymbol{q})$ is the magnetic form factor, ρ_m is the population of state m, and $\Delta_{nm} = E_n - E_m$ is the energy splitting between states n and m. The data in Figs. 6 and 7 were fitted with a Lorentzian line shape convoluted with the resolution function and Bose factor after subtracting an appropriate background of phonon spectra. From the obtained excitation energy and integrated intensity, we tried to reveal the CEF level scheme.

The key point is the strong first excitation and very weak second one. This situation can be understood in terms of the $|\pm\frac{1}{2}\rangle$ ground state with the first and the second level dominated by $|\pm\frac{3}{2}\rangle$ and $|\pm\frac{5}{2}\rangle$ states, respectively, as shown in Fig. 8. In the level scheme, we observe the strong first and weak second excitation peaks, because $\langle\pm\frac{1}{2}|J_{x,y}|\pm\frac{3}{2}\rangle$ is nonzero and $\langle\pm\frac{1}{2}|J_{x,y,z}|\pm\frac{5}{2}\rangle = 0$. The ground-state level should be $|\pm\frac{1}{2}\rangle$ because the in-plane susceptibility ($H\perp c$) is larger than the out-of-plane susceptibility ($H\|c$). The magnetic moment of the ground state, $g_J\mu_B J_z = 0.428\mu_B$, is in good agreement with the observed ferromagnetic moment of $0.41\mu_B$.

The mixing parameters a and b were estimated from the ratio of the integrated intensity of two CEF excitation peaks as $a = 0.98$ and $|b| = 0.22$. The charge distribution of each state is also shown at the right-hand site of the level scheme. The mixing of $|\pm\frac{3}{2}\rangle$ and $|\mp\frac{5}{2}\rangle$ states is so small that we cannot distinguish which state, $\Gamma_7^{(1)}$ or $\Gamma_7^{(2)}$, is the first- or second-excited level. The sign of CEF parameter B_4^4, in turn, was not determined. The CEF parameters B_n^m are listed in Table II. The CEF level scheme determined by the present neutron-scattering study is very similar to the result of the recent thermal-expansion study conducted by Takeuchi and co-workers.[8]

TABLE II. CEF parameter determined from the neutron-scattering experiment.

B_2^0	B_4^0	B_4^4
7.6 ± 0.3 K	-0.06 ± 0.04 K	$\pm0.7\pm0.1$ K

This level scheme reminds us of the quadrupolar splitting in nuclear quadrupole resonance (NQR). From the analogy of NQR, the level splitting indicates the existence of the uniaxial field gradient at the Ce site. Consequently, $|\pm\frac{1}{2}\rangle$ which has the uniaxially elongated charge distribution, as shown in Fig. 8, becomes the ground state. A similar CEF level scheme can be observed with hexagonal point symmetry which indicates the uniaxial nature.

The ground state splits into two singlets with $2\Delta\sim2T_c$ below T_c, which is consistent with the slight increase of the excitation energy, $5.9-5.2=0.7$ meV$\sim T_c$, as shown in Fig. 8.

The spin-wave excitation has been measured with the use of a single-crystalline sample. Typical constant-$\boldsymbol{q}$ spectra are shown in Fig. 9 for several $\boldsymbol{q}$ along $[h00]$. We observed a clear spin-wave excitation for $\Delta E<3$ meV. Figure 10 is the dispersion relation of the spin-wave excitation along the $[hhh]$, $[00l]$, $[h00]$, and $[hh0]$ directions. The anisotropic exchange interaction between $4f$-moments J_i in the Γ_6 ground state for the ferromagnet is introduced to account for the dispersion. The Hamiltonian for this model is described as

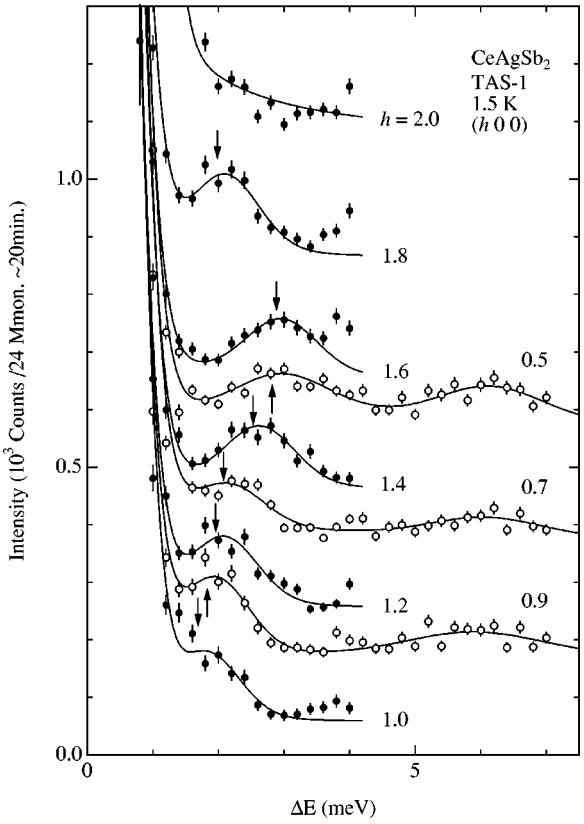

FIG. 9. Spin-wave excitation spectra in $CeAgSb_2$. The data are shifted vertically for convenience.

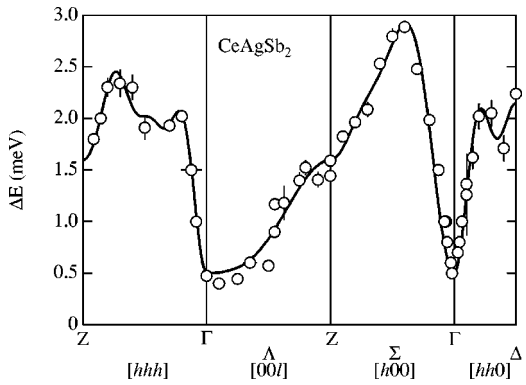

FIG. 10. Dispersion relation of the spin-wave excitation in $CeAgSb_2$. The solid line shows the calculated dispersion curve with Eqs. (8) and (9).

$$\mathcal{H}_{\rm int}=-\sum_{\langle ij\rangle}\left[I_{ij}^z J_i^z J_j^z+\frac{1}{2}I_{ij}^{\perp}(J_i^+ J_j^- + J_i^- J_j^+)\right], \tag{7}$$

where I_{ij}^z ($I_{ij}^{\perp}$) is the exchange energy for z (x,y) component of angular moment $\boldsymbol{J}$, $J^{x,y,z}$ is x,y,z component of $\boldsymbol{J}$, respectively, and $J^{\pm}=J^x\pm iJ^y$. The spin-wave dispersion relation is obtained from Eq. (7) as

$$\omega_{\boldsymbol{k}}=\Delta+\frac{9}{2}[I^{\perp}(\boldsymbol{0})-I^{\perp}(\boldsymbol{k})], \tag{8}$$

$$\Delta=\frac{1}{2}[I^z(\boldsymbol{0})-9I^{\perp}(\boldsymbol{0})], \tag{9}$$

where $I^z(\boldsymbol{k})$ and $I^{\perp}(\boldsymbol{k})$ are the Fourier transforms of I_{ij}^z and $I_{ij}^{\perp}$, respectively. The solid line in Fig. 10 is the calculated dispersion relation with Eqs. (8) and (9). We regard the crystal structure as body-centered tetragonal for simplicity. The exchange interaction $I_n^{\perp}$'s, up to 9th neighbors, were taken into account for the calculation, as shown in Fig. 11. The $I_n^{\perp}$'s obtained by fitting dispersion $I^z(\boldsymbol{0})$ and $I^{\perp}(\boldsymbol{0})$ are listed in Table III. The value of $I^z(\boldsymbol{0})$ is one order larger than that of $I^{\perp}(\boldsymbol{0})$, indicating anisotropic interaction. As clearly seen from Table III, exchange interaction is ferromagnetic, consistent with the simple ferromagnetic structure. Although the value of $I_8^{\perp}$ is negative, this component is trivial for the magnetic structure.

IV. DISCUSSION

The results of our neutron-scattering study, i.e., the absence of an antiferromagnetic/SDW peak and the spin-wave dispersion which is explained by the ferromagnetic interaction, clearly indicate that $CeAgSb_2$ has a simple ferromagnetic ordering. To date, however, a noncollinear canted antiferromagnetic structure has been proposed because of several ''unusual'' properties that were interpreted as characteristic properties of the antiferromagnetic component. In this Section, we note that these unusual properties can be explained in terms of the CEF level scheme and the simple ferromagnetic structure ordered with anisotropic exchange interaction.

The total Hamiltonian consists of the following terms:

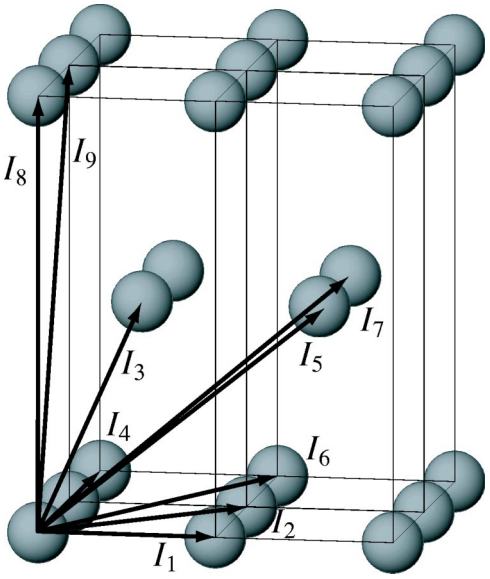

FIG. 11. Exchange interactions for the analysis of the spin-wave dispersion relation.

$$\mathcal{H}=\mathcal{H}_{\mathrm{CEF}}-g_J\mu_{\mathrm{B}}\sum_{\alpha=x,y,z}H^\alpha J^\alpha-g_J\mu_{\mathrm{B}}\sum_{\alpha=x,y,z}h^\alpha J^\alpha_{\Gamma_6}. \tag{10}$$

The first term is the CEF Hamiltonian given in Eq. (2) and the second term is the Zeeman term, while the third term describes the anisotropic exchange interaction given in Eq. (7) in the form of the mean-field approximation. The angular momentum operator $J^\alpha_{\Gamma_6}$ within Γ_6 subspace is described as

$$J^\alpha_{\Gamma_6}=O^\dagger_{\Gamma_6}J^\alpha O_{\Gamma_6}, \tag{11}$$

where O_{Γ_6} is a projection operator to the Γ_6 ground state, given by

$$O_{\Gamma_6}=\left|+\frac{1}{2}\right\rangle\left\langle+\frac{1}{2}\right|+\left|-\frac{1}{2}\right\rangle\left\langle-\frac{1}{2}\right|. \tag{12}$$

Molecular field $\boldsymbol{h}$ is described as follows:

$$h^\alpha=\lambda^\alpha\langle M^\alpha\rangle=g_J\mu_{\mathrm{B}}\lambda^\alpha\langle J^\alpha\rangle. \tag{13}$$

Mean-field parameters $\lambda^{x,y}=14$ mol/emu and $\lambda^z=167$ mol/emu were estimated from $I^\perp(\mathbf{0})$ and $I^z(\mathbf{0})$.

Figure 12 shows the temperature dependences of the magnetic susceptibilities parallel ($\chi_\parallel$) and perpendicular ($\chi_\perp$) to [001]. The magnetic susceptibility follows the Curie-Weiss law at high temperatures, and shows an anomaly at $T_c=9.6$ K, associated with the magnetic ordering. Surprisingly, $\chi_\parallel$ is much smaller than $\chi_\perp$, although the ferromagnetically ordered moment of Ce is parallel to [001]. The dotted lines show the magnetic susceptibility in the paramagnetic state, calculated with the CEF Hamiltonian using CEF parameters, as shown in Table II. These lines are basically the same as those reported by Takeuchi *et al.*[8] and Inada *et al.*,[9] although the CEF excitation energy is slightly different. The calculated susceptibility at higher temperatures is consistent with the experimental results, but the discrepancy becomes larger at lower temperatures. This discrepancy is due to the exchange interaction between Ce moments. The solid line in Fig. 12 shows the susceptibility calculated after including the anisotropic exchange interaction, as in Eq. (10). The agreement of our calculation with the experimental data is excellent. Perpendicular susceptibility $\chi_\perp$, larger than the parallel one ($\chi_\parallel$), is characteristic of the $|\pm\frac{1}{2}\rangle$ ground state because this state has larger in-plane components of J_x and J_y than J_z.

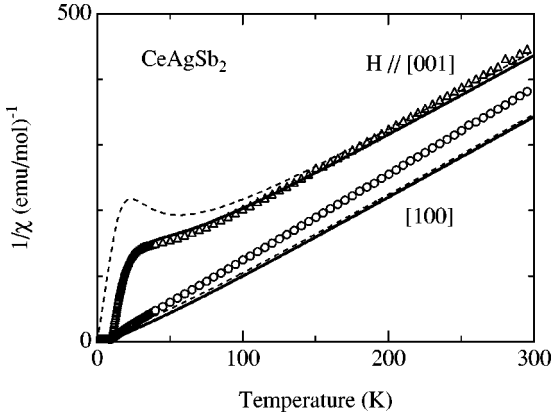

FIG. 12. Temperature dependence of magnetic susceptibility. The broken lines show the susceptibility calculated with the CEF Hamiltonian and the solid lines shows the susceptibility calculated with Eq. (10).

When the exchange interaction has a strong Ising character ($\lambda_z \gg \lambda_x$), the magnetic ordering of the z component, J_z, can take over the ordering of the in-plane components J_x and J_y. In this case, the expected values of $\langle J_x\rangle$ and $\langle J_y\rangle$ should be quantum mechanically zero, hence there is no possibility of the canting structure associated with the in-plane antiferromagnetic component.

It is particularly interesting and challenging to reproduce the CEF potential by self-consistent band calculation, which might also give an answer for the Ising character of the exchange interaction in $CeAgSb_2$.

Figure 13 shows the magnetization curves for the fields parallel ($H_\parallel$) and perpendicular ($H_\perp$) to [001]. Magnetization for $H_\parallel$ shows a sharp ferromagnetic hysteresis curve with the spontaneous moment of $0.4\mu_{\mathrm{B}}$, while the hard-axis magnetization increases with $H_\perp$ more than the spontaneous moment along [001], and saturates at $1.3\mu_{\mathrm{B}}$ for $H>3$ T. Historically, the existence of a large antiferromagnetic component has been speculated from these magnetization curves. However, these magnetization curves can be explained with

TABLE III. Exchange interaction $I^\perp_n$ in $CeAgSb_2$.

$I^\perp_1$	18 ± 4 μeV	$I^\perp_6$	7 ± 2 μeV
$I^\perp_2$	31 ± 3 μeV	$I^\perp_7$	5 ± 1 μeV
$I^\perp_3$	5 ± 2 μeV	$I^\perp_8$	-9 ± 5 μeV
$I^\perp_4$	5 ± 3 μeV	$I^\perp_9$	~0 μeV
$I^\perp_5$	~0 μeV	Δ	500 μeV
$I^z(\mathbf{0})$	3.95 ± 0.04 meV	$I^\perp(\mathbf{0})$	0.33 ± 0.04 meV

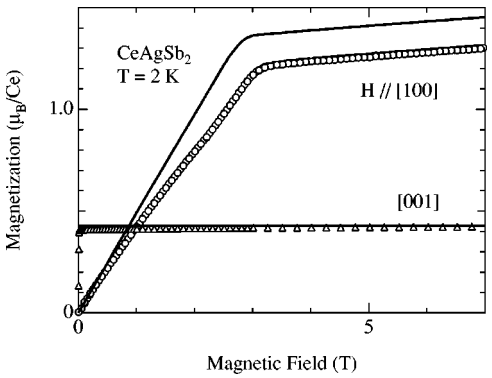

FIG. 13. Magnetization curves for the fields parallel ($H_{\|}$) and perpendicular ($H_{\perp}$) to [001]. The solid lines show values calculated with Eq. (10).

Eq. (10), which implies a simple ferromagnetic ground state. The larger magnetization perpendicular to the *c* axis is characteristic of ground state $|\pm\frac{1}{2}\rangle$. In the $|\pm\frac{1}{2}\rangle$ ground state, a large in-plane component $J_{x,y}$ can be induced with the application of $H_{\perp}$. Meanwhile, the easy-axis magnetization shows no gradual change with $H_{\|}$ but sudden change is expected at a much higher critical field $H \approx 110$ T, where the crossover of the ground state takes place due to the Zeeman energy.[8]

The in-plane magnetization curve, with the application of $H\|$ [100], shows a saturation tendency above critical field H_c, denoted by arrows in Fig. 14. Critical field H_c decreases with increasing temperature. In Fig. 15, $H_c(T)$ is plotted as a function of temperature.

The closed marks in Fig. 14 show the ferromagnetic moment along [001], with the magnetic field parallel to [110] measured from the neutron diffraction intensity at the (110) peak position. With this configuration, the in-plane magnetization does not contribute to any magnetic scattering, because the induced in-plane magnetic moment is parallel to scattering vector $\boldsymbol{q}$. Therefore, only the ferromagnetic component along [001] is observed.

The ferromagnetic component along [001] exhibits a gradual decrease with increasing in-plane magnetic field, and disappears at critical field H_c, where the in-plane magnetic moment shows a kink behavior. Our data indicate that H_c is

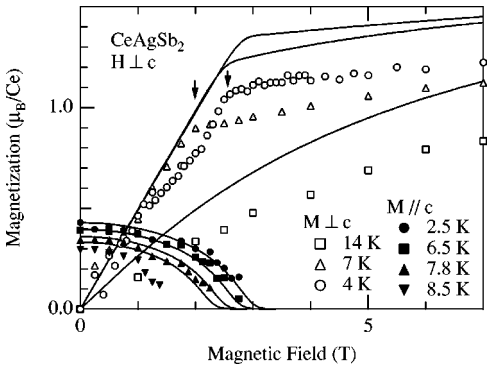

FIG. 14. In-plane magnetization ($M\perp c$) and the ferromagnetic moment ($M\|c$) are plotted as a function of magnetic field perpendicular to [001].

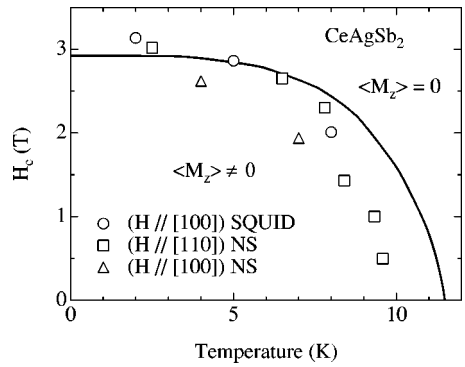

FIG. 15. Critical field $H_c(T)$ for the field perpendicular to [001]. The solid line shows H_c calculated using Eq. (10).

the field where the ferromagnetic moment switches its direction from parallel to perpendicular, relative to [001]. This switching corresponds to the crossover of the ground state from $|+\frac{1}{2}\rangle$ to the linear combination of $|\pm\frac{1}{2}\rangle$. It is the reason why a kink is observed in the magnetization curve for the field direction perpendicular to [001]. Furthermore, these magnetization curves can be understood in terms of Eq. (10). Critical field $H_c(T)$ can also be explained by the same Hamiltonian, as shown by a solid line in Fig. 15.

Metamagnetic transition driven by the rotation of the quadrupole moment has been reported in $PrCu_2$ by Settai *et al.*[19] On the contrary, quadrupole moment $\boldsymbol{O}_2^0$ in $CeAgSb_2$ has a finite expected value even in the paramagnetic phase, and in the ferromagnetic state $\langle \boldsymbol{O}_2^0 \rangle$ stays almost constant below and above $H_c(T)$. Therefore, the quadrupole moment, in the case of $CeAgSb_2$, is not important to the magnetization process of this compound.

Adroja *et al.*[16] reported that the magnetostriction along the field direction perpendicular to [001] exhibits a broad peak around critical field H_c. This broad peak is also explained by Eq. (10). The magnetic contribution to the strain is expressed as follows:[20]

$$\varepsilon_{xx} = A_{xx}\langle \boldsymbol{O}_2^0 \rangle + B_{xx}\langle \boldsymbol{O}_2^2 \rangle. \tag{14}$$

Perpendicular field ($H_{\perp}$) dependences of $\langle \boldsymbol{O}_2^0 \rangle$ and $\langle \boldsymbol{O}_2^2 \rangle$ are plotted in Fig. 16. The expected value $\langle \boldsymbol{O}_2^0 \rangle$ increases

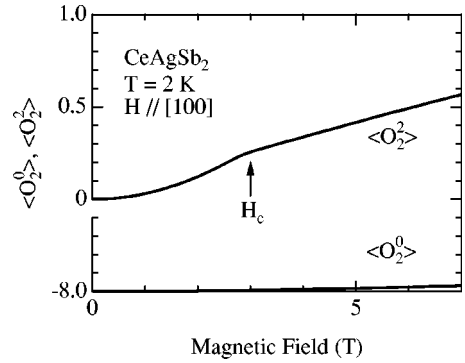

FIG. 16. Magnetic-field dependence of the expected value of the quadrupolar operator $\langle \boldsymbol{O}_2^0 \rangle$ and $\langle \boldsymbol{O}_2^2 \rangle$ at 2 K for the field along the *a* axis.

smoothly with the field, while $\langle O_2^2 \rangle$, which is zero without $H_\perp$ because of the tetragonal symmetry, shows a kink at H_c. Therefore, the kink observed by Adroja *et al.* is caused by the second term of Eq. (14).

Inada *et al.*[9] reported that specific heat $C(\mathrm{CeAgSb_2}) - C(\mathrm{LaAbSb_2})$, showing $T^{3/2}$ dependence at low temperatures, below 1.5 K, is consistent with the ferromagnetic spin wave.

It should be noted that $CeAgSb_2$ exhibits a huge resistivity drop of the order of 10^{-3} below T_c. Since the resistivity drop is accompanied by the magnetic ordering, it is clear that this phenomenon should be explained with a scenario based on a weak p-f mixing between localized-4f electrons in the $|J_z = \pm\frac{1}{2}\rangle$ doublet and p electrons on p_x and p_y orbitals of Sb^{2-} ions at Sb(2) sites.

The huge resistivity drop, such as at a metal-insulator transition, associated with ferromagnetic ordering, is reminiscent of, for example, the double-exchange mechanism in Mn compounds. It will be satisfying when the resistivity drop below T_c and the strong anisotropic interaction can be explained consistently by the p-f hybridization based on the simple CEF level scheme with ground state $|\pm\frac{1}{2}\rangle$ and p_σ orbitals. The occurrence of the Kondo effect with $T_K = 80$ K is suggested by the results of thermopower and inelastic neutron scattering.[21] Moreover, the relatively large specific coefficient $\gamma = 46$ mJ/K^2 mol also suggests the existence of the Kondo effect. However, we are unsure whether the Kondo effect could exist in a ferromagnetic localized-4f system without moment reduction.

In conclusion, our neutron-scattering study revealed the crystal structure, crystalline electric-field level scheme, and the simple ferromagnetic structure of $CeAgSb_2$. The crystal structure is described by Sologub's model. The CEF level scheme consists of the $|\pm\frac{1}{2}\rangle$ ground state and the first and second excited levels dominated by $|\pm\frac{3}{2}\rangle$ and $|\pm\frac{5}{2}\rangle$, respectively. We showed that the magnetic properties of $CeAgSb_2$ can be well understood in terms of the $|\pm\frac{1}{2}\rangle$ ground state with anisotropic ferromagnetic exchange interaction.

ACKNOWLEDGMENTS

The authors would like to thank T. Takeuchi, T. Takimoto, K. Kubo, Y. Inada, and K. Sugiyama for stimulating discussions. We also thank Y. Koike and K. Kaneko for their technical assistance. Part of this work was financially supported by a Grant-in-Aid for COE Research (10CE2004) from the Ministry of Education, Culture, Sports, Science and Technology of Japan.

*Present address: Graduate School of Science, Osaka University, Osaka, Toyonaka 560-0043, Japan. Electronic address: araki@nano.phys.sci.osaka-u.ac.jp

[1] V.L. Ginzburg, Zh. Eksp. Teor. Fiz. **31**, 202 (1956) [Sov. Phys. JETP **4**, 153 (1957)].

[2] S.S. Saxena, P. Agarwal, K. Ahllan, F.M. Grosche, R.K.W. Haselwimmer, M.J. Steiner, E. Pugh, I.R. Walker, S.R. Julian, P. Monthoux, G.G. Lonzarich, A. Huxley, I. Sheikin, D. Braithwaite, and J. Flouquet, Nature (London) **406**, 587 (2000).

[3] D. Aoki, A. Huxley, E. Ressouche, D. Braithwaite, J. Flouquet, J.-P. Brison, E. Lhotel, and C. Paulsen, Nature (London) **413**, 613 (2001).

[4] G. André, F. Bourée, M. Kolenda, B. Leśniewska, A. Oleś, and A. Szytuła, Physica B **292**, 176 (2000).

[5] Y. Muro, N. Takeda, and M. Ishikawa, J. Alloys Compd. **257**, 23 (1997).

[6] M. Nakashima, S. Kirita, R. Asai, T.C. Kobayashi, T. Okubo, M. Yamada, A. Thamizhavel, Y. Inada, R. Settai, A. Galatanu, E. Yamamoto, T. Ebihara, and Y. Onuki, J. Phys.: Condens. Matter **15**, L111 (2003).

[7] K.D. Myers, S.L. Bud'ko, I.R. Fisher, Z. Islam, H. Kleinke, A.H. Lacerda, and P.C. Canfield, J. Magn. Magn. Mater. **205**, 27 (1999).

[8] T. Takeuchi, A. Thamizhavel, T. Okubo, M. Yamada, N. Nakamura, T. Yamamoto, Y. Inada, K. Sugiyama, A. Galatanu, E. Yamamoto, K. Kindo, T. Ebihara, and Y. Onuki, Phys. Rev. B **67**, 064403 (2003).

[9] Y. Inada, A. Thamizhavel, H. Yamagami, T. Takeuchi, Y. Sawai, S. Ikeda, H. Shishido, T. Okubo, M. Yamada, K. Sugiyama, N. Nakamura, T. Yamamoto, K. Kindo, T. Ebihara, A. Galatanu, E. Yamamoto, R. Settai, and Y. Onuki, Philos. Mag. B **82**, 1867 (2002).

[10] O. Sologub, H. Noël, A. Leithe-Jasper, P. Rogl, and O.I. Bodak, J. Solid State Chem. **115**, 441 (1995).

[11] M. Brylak, M.H. Möller, and W. Jeitschko, J. Solid State Chem. **115**, 305 (1995).

[12] O. Sologub, K. Hiebl, P. Rogl, H. Nöel, and O. Bodak, J. Alloys Compd. **210**, 153 (1994).

[13] F. Izumi and T. Ikeda, Mater. Sci. Forum **321-324**, 198 (2000).

[14] S.-i. Fujimori, T. Okane, J. Okamoto, K. Mamiya, Y. Muramatsu, A. Fujimori, H. Yamagami, A. Thamizhavel, T. Ebihara, and Y. Onuki (unpublished).

[15] J.A. Dann, A.D. Hillier, J.G.M. Armitage, and R. Cywinski, Physica B **289-290**, 38 (2000).

[16] D.T. Adroja, P.C. Riedi, J.G.M. Armitage, and D. Fort, Acta Phys. Pol. B **34**, 945 (2003).

[17] M. T. Hutchings, in *Solid State Physics: Advances in Research and Applications*, edited by F. Seitz and B. Turnbull (Academic, New York, 1965), Vol. 16, p. 227.

[18] K.W.H. Stevens, Proc. Phys. Soc., London, Sect. A **65**, 209 (1952).

[19] R. Settai, S. Araki, P. Ahmet, M. Abliz, K. Sugiyama, Y. Onuki, T. Goto, H. Mitamura, T. Goto, and S. Takayanagi, J. Phys. Soc. Jpn. **67**, 636 (1998).

[20] P. Morin, J. Rouchy, and D. Schmitt, Phys. Rev. B **37**, 5401 (1988).

[21] M. Houshiar, D.T. Adroja, and B.D. Rainford, J. Magn. Magn. Mater. **140-144**, 1231 (1995).